Nanoscale
Advances

PAPER

View Article Online
View Journal | View Issue

Cite this: *Nanoscale Adv.*, 2025, 7, 7987

A novel anodic nanostructured stainless steel-304L oxide as an emerging electrode material for high energy density asymmetric supercapacitors: experimental and DFT insights

Jawad Ahmad,†[a] Muhammad Danish,†[a] Ghafar Ali, *[a] Maaz Khan, [a] Shahzad Anwar,[b] Gul Rahman,[c] Mashkoor Ahmad, [a] Yi Xie, [d] Seunguk Cheon,[e] Sung Oh Cho *[e] and Imran Shakir[f]

The electrode material plays a significant role in the performance of supercapacitors. Therefore, the development of a novel electrode material for high energy density, high power density, and stable supercapacitors is highly desirable. The emergence of the stainless steel 304L (SUS-304L) oxide nanostructure as an electrode material provides an opportunity to explore its supercapacitive behavior. In the present study, a simple and facile technique of anodization was employed to synthesize nanostructured SUS-304L oxide (in powder form), which would be otherwise impossible to achieve using the existing synthetic routes. The structural and microscopic results confirm the formation of multiple phases (Fe_2O_3, Fe_3O_4, and $NiCr_2O_4$), the polycrystalline behavior, and a morphology in which the nanoparticles (NPs) overlap nanosheets (NSs). As an electrode, the developed material demonstrated excellent electrochemical performance, achieving a high specific capacitance of ~1226 F g^{-1} at 2 A g^{-1} in a KOH electrolyte. The fabricated asymmetric supercapacitor device (SUS-304L oxide//activated carbon) exhibited a specific capacitance of ~209 F g^{-1} and an energy density of ~29 Wh kg^{-1} at a power density of ~751 W kg^{-1}. Additionally, the device retained ~89% of its initial capacitance over 8000 cycles. The outstanding performance is due to the synergetic effect of the multiple phases. To further elucidate the supercapacitive behavior, *ab initio* calculations based on density functional theory (DFT) were used to determine the quantum capacitance. The observed large capacitance is mainly contributed by Fe-oxides and can be ascribed to the large density of states of minority spin states of t_{2g} and e_g orbitals of Fe atoms at the octahedral sites. These findings demonstrate the potential of the prepared composite nanostructure (SUS-304L oxide) as a high-performance electrode material for practical asymmetric supercapacitor applications.

Received 24th June 2025
Accepted 25th September 2025

DOI: 10.1039/d5na00618j

rsc.li/nanoscale-advances

1. Introduction

In the past few decades, rapid societal development, environmental pollution, and the depletion of fossil fuels have created serious challenges. To address the growing energy crisis, scientists and researchers have developed various energy storage devices, including batteries, fuel cells, flywheels, and supercapacitors.[1,2] Among these, supercapacitors have emerged as a promising solution due to their fast charge–discharge capabilities, high power density, and long cycle life compared to conventional capacitors and batteries. They hold great potential in applications such as automobiles, uninterruptible power supply backup systems, and consumer electronics.[3–5] However, supercapacitors still face challenges, including poor stability and low energy density, which limit their widespread practical applications. Developing advanced electrode materials with superior electrochemical properties could help to overcome these limitations and enhance their performance.

The performance of a supercapacitor is highly dependent on the electrode material; therefore, selecting the appropriate electrode material is crucial for optimizing its efficiency. Various electrode materials with high redox activity and

---

[a] *Nanomaterials Research Group, Physics Division, PINSTECH, Islamabad 45650, Pakistan. E-mail: ghafarali@kaist.ac.kr; ghafarali@gmail.com*
[b] *Physics Department, Islamia College University Peshawar, KPK, Pakistan*
[c] *Physics Department, Quaid-i-Azam University, Islamabad 45320, Pakistan*
[d] *State Key Laboratory of Silicate Materials for Architectures, Wuhan University of Technology, No. 122, Luoshi Road, Wuhan 430070, China*
[e] *Department of Nuclear and Quantum Engineering, Korea Advanced Institute of Science and Technology (KAIST), 291 Daehak-ro, Yuseong-gu, Daejeon 34141, Republic of Korea. E-mail: socho@kaist.ac.kr*
[f] *Department of Physics, Faculty of Science, Islamic University of Madinah, Madinah 42351, Saudi Arabia*

† Both authors have equal contributions.

structural stability have been explored for supercapacitor applications. These materials include carbon-based compounds, transition metal-oxides (TMOs), sulfides, phosphides, and hydroxides.[6–9] Additionally, metal–organic frameworks and conducting polymers have emerged as attractive alternatives.[10] In this regard, developing efficient, robust, and inexpensive electrode materials using earth-abundant elements is essential for energy storage devices. To date, various TMOs such as NiO, CoO, RuO_2, Fe_2O_3, CuO, V_2O_5, MnO_2, and Co_2O_3 have demonstrated exceptional theoretical capacitance and significantly influenced the overall performance of supercapacitors. However, despite the promising properties, their practical application is limited by high costs and restricted availability.[11–17] Among the TMOs, iron (Fe)-based electrodes have gained attention due to their abundant availability, impressive theoretical potential, and cost-effectiveness.[18] Recently, a few Fe-based alloys such as Fe–Co–Ni–Cu–Zn,[19] Co–Cr–Ni–Fe–Mn,[20] Fe–Cr,[21] and NiFe–graphene[22] have been synthesized using complex processes and investigated for supercapacitor applications.

Among the various Fe-based alloys, SUS-304L oxide has emerged as a favorable and effective material for electrochemical charge storage due to its cost-efficiency, high corrosion resistance, good mechanical strength, and excellent stability. It primarily consists of Fe, along with other low wt% elements as given in Table 1. Despite its promising properties, nanostructured SUS-304L oxide has been scarcely investigated as an efficient electrode material for supercapacitors. Various methods, including hydrothermal, solvothermal, thermal oxidation, co-precipitation, CVD, electrochemical deposition, *etc.*, are being used to synthesize different TMOs nanostructured for energy storage devices. However, these methods have some limitations, incorporate impurities in the final product, and cannot be employed to obtain an oxide nanostructure of an alloy. Anodization is an alternative, which is considered superior due to its simplicity, versatility, efficiency, cost-effectiveness, environmental friendliness, and single-step process compared to the complicated fabrication techniques.

Depending on the nature of the electrolyte, anodization can convert metal and alloy into their oxide nanostructures, producing either a thin film[23,24] adhered strongly to the substrate, or a powder[23,25] accumulated at the bottom of the electrochemical cell. Interestingly, for the same material (titanium), we found that one electrolyte produced a thin film (TiO_2 nanotubes)[24] that remains bonded to the Ti-substrate, while another electrolyte (aqueous KCl/NaCl) results in TiO_2 nanoparticles (NPs) accumulating at the bottom of the cell.[25] In the former case, the anode remains intact and does not dissolve, whereas in the latter case, the anode is completely dissolved (sacrificial) and transformed into oxide nanostructures (in powder form). It is well known that anodization in a chloride-free electrolyte always leads to the formation of a thin oxide film that is strongly attached to the metal substrate. The anion species (O^{2-} and OH^-) generated as a result of water electrolysis diffuses towards the anode due to the applied voltage, reacting with metal cations and forming an oxide layer on the surface of the substrate. Recently, we have obtained an ideal self-organized, highly ordered, and hexagonal nanoporous oxide layer (thin film) on a large scale when we anodized SUS-304L in ethylene glycol-based electrolyte.[26] Similarly, for the first time, we have also produced various metals and alloy-oxide NPs in bulk quantities *via* anodization in aqueous NaCl or KCl electrolyte.[27]

Inspired by our previous work on Ti anodized in two different electrolytes, herein, we have anodized SUS-304L in an aqueous KCl/NaCl electrolyte for powder production instead of the thin oxide film obtained in ethylene glycol electrolyte as reported in our previous work.[26] This study presents the supercapacitor application of nanostructured SUS-304L oxide composed of NPs overlapping nanosheets, produced *via* the straightforward anodization technique. To the best of our knowledge, nanostructured SUS-304L oxide (in powder form) has not been previously explored for energy storage purposes. The prepared material was subjected to various structural, morphological, and electrochemical studies and has demonstrated high specific capacitance, high energy density, high power density, and outstanding cyclic stability. These remarkable findings make SUS-304L-based functional materials promising candidates for next-generation electrochemical energy storage devices.

2. Experimental procedure

2.1. Materials and chemicals

The SUS-304L sheet (0.1 mm thickness, 99.99% purity) was purchased from Nilaco Corporation, Japan. Ni-sheets, Ni-foam, and Al-foils were obtained from Goodfellow, England, UK. Reagent-grade sodium chloride (NaCl, 99.99% purity), sulfuric acid (H_2SO_4, 98% purity), potassium hydroxide (KOH, 99.99% purity), acetone, and ethanol were purchased from Sigma-Aldrich, USA. All the electrolytes were prepared using deionized (DI) water.

2.2. Anodization of SUS-304L and the formation of multiple metal oxides

Before anodization, SUS-304L sheets were cleaned by sonicating in acetone and ethanol, respectively, for 5 min each, followed by rinsing with D.I water and drying in an oven at 60 °C.

Table 1 Composition of the stainless steel-304L (SUS-304L)

Elements	Cr	Ni	Mn	C	N	P	Si	S	Fe
wt%	18.00–20.00	8.00–12.00	2.00	0.03	0.10	0.045	0.75	0.030	Balance

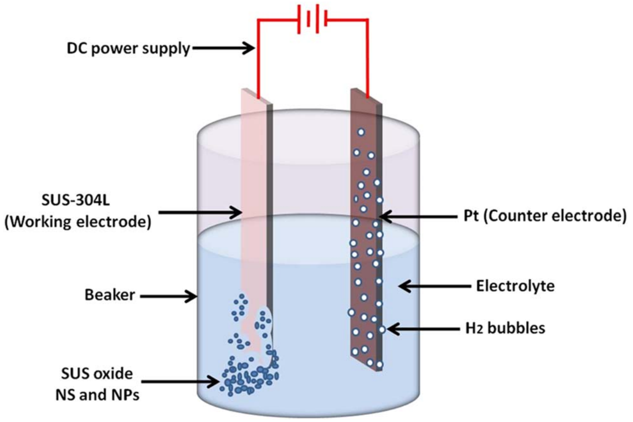

Fig. 1 Schematic showing the experimental set-up for the production of the nanostructured SUS-304L oxide (NPs overlapped with NSs) in 1 M NaCl electrolyte at room temperature.

Anodization was performed in a home-made two-electrode system with a platinum plate (15 × 25 × 0.2 mm^3) as the cathode and SUS-304L sheet as the anode as shown in Fig. 1. Anodization was conducted at constant voltage (10 V) in 1 M aqueous NaCl electrolyte under continuous magnetic stirring at room temperature using a programmable DC power supply (Tektronix PWS 4305, USA). Oxide precipitates were formed as result of SUS-304L sheet (sacrificial anode) dissolution along with the strong evolution of H_2 at the cathode when the power supply was turned ON. The whole SUS-304L sheet was converted into solid precipitates that settled at the bottom of the electrochemical cell during the anodizing period. Thus, anodization in 1 M NaCl electrolyte converted the entire SUS-304L sheet into SUS-304L oxide powder, unlike the formation of the nanostructured oxide layer (thin film) adhered to the surfaces of metals and alloys in organic-based electrolytes.[28,29] These results reveal that the nature of the material can be tailored from thin film formation to powder formation of the same materials by just changing the type of electrolyte.

The resultant precipitates were first dispersed and sonicated in DI water using an ultra-sonication bath (Elma E60H, Germany) for 5 min, and then collected *via* centrifugation. This cycle was repeated seven times to ensure the complete removal of salt (NaCl) if incorporated by the electrolyte. Consequently, the precipitates were kept in an oven at 70 °C overnight, and the dried product was collected and ground to obtain a fine powder. The obtained SUS-304L oxide fine powder was then annealed at 500 °C for 2 h at a heating rate of 3 °C min^{-1} and then cooled to room temperature.

2.3. Preparation of electrodes

Ni-foam was activated in diluted H_2SO_4 by sonicating for 30 min, followed by sonication in ethanol and D.I water, respectively, for 15 min each. Subsequently, the SUS-304L oxide powder, carbon black, and poly(vinylidene fluoride-hexafluoropropylene) (PVDF-HFP, used as a binder) were mixed in the weight ratio of 70 : 20 : 10 with the addition of a few drops of *N*-methylpyrrolidone (NMP). In order to obtain a homogeneous slurry, the mixture was stirred for 24 h and then coated (∼1.0 mg) on Ni-foam (active surface area = ∼0.5 cm^2) and dried in a vacuum drying oven at 60 °C for 24 h. Fig. S1 shows a schematic illustration of the whole process from the synthesis of the material to electrochemical measurements.

2.4. Fabrication of the SUS oxide//activated carbon asymmetric supercapacitor device

An asymmetric supercapacitor (ASC) device was fabricated by combining the electric double layer capacitor (EDLC)-type activated carbon (negative electrode) and faradaic type SUS-304L oxide comprised of nanostructured Fe_2O_3, Fe_3O_4, and $NiCr_2O_4$ (positive electrode). The EDLC will provide a higher power density, whereas the faradaic-type material will provide a high energy density to the device.[30] The nanostructured SUS-304L oxide slurry was coated on a Ni-sheet (0.1 mm thickness) to obtain the positive electrode while the slurry (containing 75 wt% activated carbon and 25 wt% PVDF-HFP) was coated over the Al-foil to prepare the negative electrode for the device fabrication.[31] Ni-sheet, Al-foil, Whatman filter paper, and PVA/KOH gel were used as the current collectors, separator, and electrolyte for the asymmetric supercapacitor, respectively. The PVA/KOH gel electrolyte was prepared by mixing 5.6 g KOH with 6 g PVA in 50 mL of DI water, and heated at 90 °C for 4 h under continuous stirring. The size of the fabricated device was 1 × 1 cm^2, which was employed to light commercially available LEDs. Fig. S2 exhibits the schematic diagram of the fabricated device.

2.5. Characterizations

The crystal structure and phase purity of the samples were studied using GAXRD (Rigaku D/MAX 2500 V diffractor, Japan) with a Cu Kα source ($\lambda = 1.5418$ Å) at 40 kV. The surface morphology and elemental composition were investigated using FESEM (UHR-SEM Magellan 400, FEI, USA) and TEM (Tecnai G2 F30, FEI, USA). Energy dispersive X-ray (EDX) spectra were recorded with the help of FESEM, and selected area electron diffraction (SAED) patterns were obtained with TEM. X-ray photoelectron spectroscopy (XPS) analysis was carried out using a spectrometer (Sigma Probe, Thermo VG Scientific) with an Al Kα excitation source operated at 15 kV and 7 mA. The XPS spectra were recorded with a pass energy of 50 eV, a source angle of 30°, and an analyzer angle of 40°. The binding energies were calibrated using the C 1s peak (∼285.5 eV) resulting from adventitious hydrocarbon contamination. Fourier-transform infrared (FTIR) spectroscopy was performed using a Nicolet iS50 FTIR spectrometer. FTIR spectra were recorded in the range of 4000–400 cm^{-1}.

2.6. Electrochemical measurements

The electrochemical measurements were performed using an electrochemical workstation (CHI660E, China) in a basic aqueous electrolyte (1 M KOH). In a three-electrode system, the developed material deposited on Ni-foam was used as the working electrode, a platinum electrode was used as the counter electrode, and the $Hg/HgCl_2$ electrode as a reference electrode.

The cyclic voltammetry (CV) measurements were carried out at different scan rates (10–50 mV s^{-1}) with a voltage window of −0.1 to 0.6 V. The galvanostatic charge–discharge (GCD) measurements were performed at a current density in the range of 2–8 A g^{-1} with a voltage window of 1 to 0.45 V. The electrochemical impedance spectroscopy (EIS) measurements were conducted in the frequency range of 0.1 Hz to 140 kHz. All the electrochemical measurements were recorded at room temperature. The performance of the fabricated ASC was also studied by CV and GCD in the potential window of 0 to 1 V in PVA/KOH gel electrolyte using a two-electrode system. EIS analysis of the ASC device was conducted in the same frequency range.

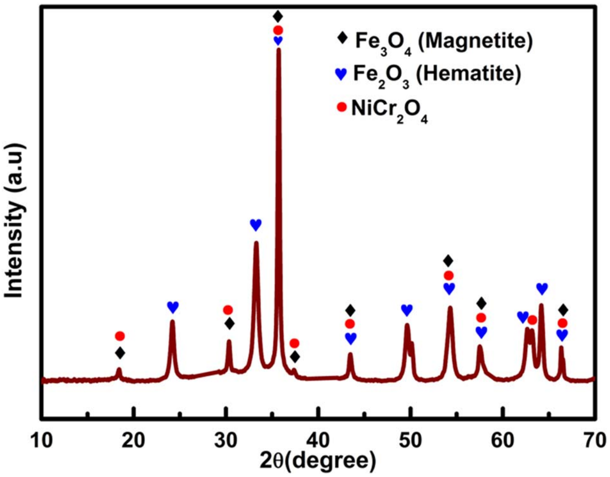

Fig. 2 XRD pattern of the anodic nanostructure of the SUS-304L oxide annealed at 500 °C in air for 2 h, showing the formation of multiple phases.

The specific capacitance, energy density, and power density of the fabricated electrode and device were calculated using the following eqn (1)–(3):

$$C_s = \frac{I \times \Delta t}{m \times \Delta V} \tag{1}$$

where 'C_s' is the specific capacitance of the electrode, I is the discharging current, m is the mass of the active materials, ΔV represents the discharging potential window, and Δt is the discharging time.

$$E_d = \frac{C_s \times V^2}{7.2} \tag{2}$$

Here, E_d represents the energy density, C_s is the specific capacitance, and V is the potential window.

$$P_d = \frac{3600 E_d}{\Delta t} \tag{3}$$

Here, P_d denotes power density, E_d is energy density, and Δt represents discharging time.

3. Results and discussion

3.1. Structural, morphological, and compositional analyses

The structural and crystallographic studies of nanostructured SUS-304L oxide were investigated using XRD, as shown in Fig. 2. The diffraction pattern shows the formation of hematite (Fe_2O_3), magnetite (Fe_3O_4), and nichromite ($NiCr_2O_4$) phases. The diffraction peaks observed at ∼24.1°, 33.2°, 35.7°, 43.5°, 49.5°, 54.1°, 57.5°, 62.5°, 64.1°, and 66.4 can be assigned to the (012), (104), (110), (202), (024), (116), (018), (214), (300), and (125) planes of the hexagonal phase of Fe_2O_3 (ICDD card #89-0599), respectively. The well-defined peaks at around 18.5°, 30.4°, 35.7°, 37.4°, 43.5°, 54.1°, 57.5°, and 66.4° correspond to

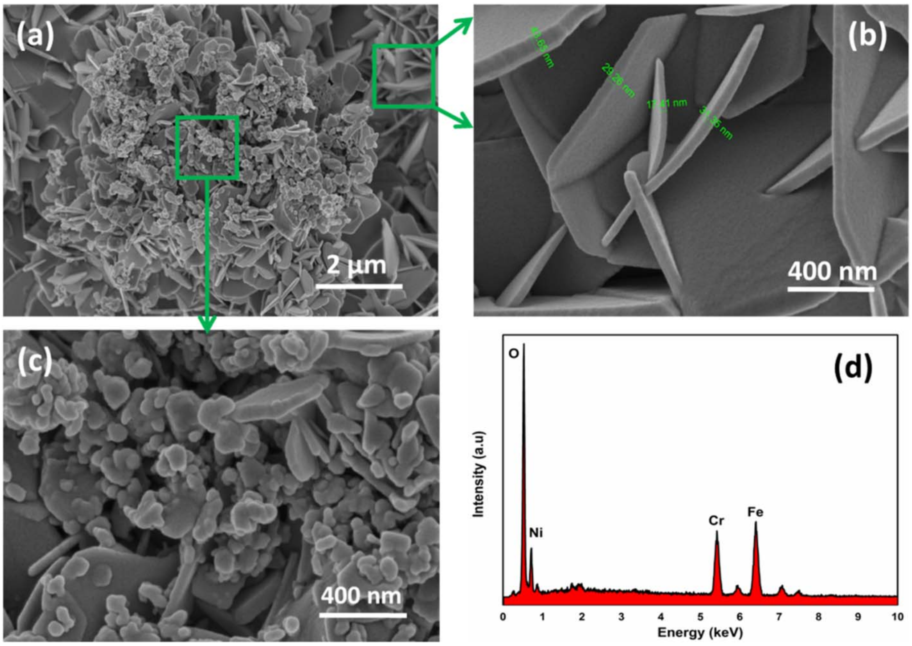

Fig. 3 (a–c) FESEM images of the nanostructured SUS-304L oxide at different magnifications, along with its (d) EDX spectrum.

the (111), (220), (311), (222), (400), (422), (511), and (531) miller indices of the cubic structure of Fe_3O_4 (ICDD card #75-0449). Moreover, peaks related to the $NiCr_2O_4$ cubic structure were also observed at 18.5°, 30.4°, 35.7°, 37.4°, 43.5°, 54.1°, 57.5°, 63.2°, and 66.4°, corresponding to the (111), (220), (311), (222), (400), (422), (511), (440), and (531) planes (ICDD card #75-0198), respectively. No impurity was found in the XRD pattern, reflecting the advantage of anodization over other synthetic routes used for nanomaterial preparation. Our XRD results revealed that the anodization of the alloy (SUS-304L) leads to the formation of multiple phases of the constitutional elements, as described above. Furthermore, the narrow and sharp XRD peaks suggest the outstanding crystallinity of the prepared material.

The morphology of the nanostructured SUS-304L oxide was investigated using FESEM, as shown in Fig. 3. Notably, the low magnification image (Fig. 3a) clearly shows the formation of the nanostructure comprised of NPs overlapping the two-dimensional (2D) entangled NSs. The NPs are dispersed non-homogeneously on the surface of NSs. The high-magnification image of the entangled NSs is shown in Fig. 3b, with an average thickness of approximately 30 nm. These self-organized NSs are entangled with each other in such a way that they provide additional sites for reaction and storage compared to the plain nanostructure morphology.[32,33] This type of morphology is very useful in applications due to its high surface area compared to other morphologies.[34] Such a structure provides a large electroactive surface for faradaic reactions due to its high surface area. It is worth mentioning that the entangled NSs did not separate from each other despite several applications of sonication. In our recent articles, we observed the self-organized formation of the hierarchical 3D-nanoflower morphology of iron oxide and MgO-entangled NSs *via* the anodization of Fe and Mg sheets, respectively, in organic-based electrolytes. Similarly, the anodization of metals or alloys in aqueous NaCl or KCl electrolytes generally produced homogeneous and spherical NPs as reported in our patent.[35] Fig. 3c shows the magnified image of an area containing NPs overlapping NSs, exhibiting the spherical morphology. The chemical composition of nanostructured SUS-304L oxide was determined by EDX. The EDX spectrum (Fig. 3d) shows the peaks of O, Ni, Cr, and Fe, which are the main constituents of SUS-304L, as given in Table 1. The EDX results are well-matched with XRD data, confirming that the prepared material is free from impurity. The structural morphology of the samples was also investigated using HRTEM. The low-resolution TEM image (Fig. 4a) also exhibits the simultaneous formation of 2D NSs and NPs, which is in good agreement with the FESEM results (Fig. 3a). The 2D NSs exhibit different morphologies, like square, rectangular, and irregular. Fig. 4b reveals the high-resolution TEM image of an individual 2D nanosheet with an irregular morphology. The boundaries, along with diffraction fringes, can be seen clearly in the image. The predominant

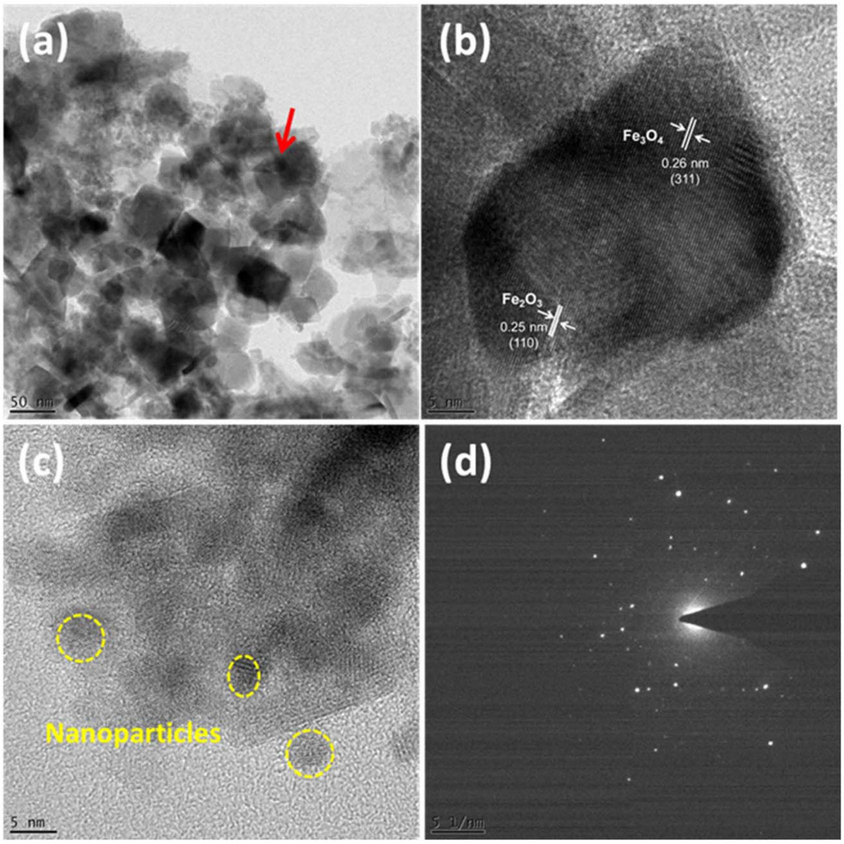

Fig. 4 (a–c) HRTEM images of the nanostructured SUS-304L oxide at different resolutions, along with its (d) SAED pattern.

observation of the crystal planes shows the excellent crystallinity of the samples. The HRTEM image of NPs (Fig. 4c) further confirmed the FESEM results, where the individual NPs with spherical morphology can be observed. These NPs are well separated from each other, and most of the particles can be seen separately without any agglomeration, as shown by the marked area in Fig. 4c. The average diameter of a NP is around 12 nm. The SAED pattern (Fig. 4d) shows the diffraction spots confirming that the nanostructured SUS-304L oxide is polycrystalline in nature.

The XPS survey spectrum of the nanostructured SUS-304L oxide (Fig. S3) shows the peaks of Ni, Fe, Cr, O, and C elements, which further confirmed the high purity of the developed material. The high-resolution XPS spectrum of Ni 2p peaks is presented in Fig. 5a. The two major peaks at 853.1 eV and 870.3 eV were assigned to Ni $2p_{3/2}$ and Ni $2p_{1/2}$, along with two shake-up satellite peaks at 860.8 and 879.8 eV. The difference in binding energies of Ni $2p_{3/2}$ and Ni $2p_{1/2}$ is 17.2 eV, thus indicating that Ni is in the +2 oxidation state. The high-resolution XPS spectrum of Cr 2p (Fig. 5b) exhibits two peaks at 577.7 eV (Cr $2p_{3/2}$) and 587.3 eV (Cr $2p_{1/2}$). The energy separation between Cr $2p_{3/2}$ and Cr $2p_{1/2}$ is approximately 9.6 eV, suggesting Cr in the +3 oxidation state. The presence of Ni^{2+} and Cr^{3+} confirmed the formation of the $NiCr_2O_4$ structure.[35] The two main peaks at about 710.56 eV and 723.7 eV in the deconvoluted Fe 2p spectrum can be assigned to Fe $2p_{3/2}$ and Fe $2p_{1/2}$, which correspond to iron oxide.[32,36] Furthermore, the presence of a satellite peak at ~717.5 eV confirmed the co-existence of hematite and magnetite phases, thus further supporting the XRD results, in line with our previous report.[32] The deconvoluted high-resolution XPS spectrum of O 1s revealed the binding energy peak at 528.1 eV, attributed to the contribution of lattice oxygen.[37]

In order to determine the presence of functional groups, FTIR spectra of nanostructured SUS-304L oxide were recorded in the range of 4000–400 cm^{-1} as shown in Fig. S4. The broad band at ~3404 cm^{-1} in the spectrum is due to the stretching vibration of the OH group.[38] The band around 1625 cm^{-1} shows the existence of H–O–H bending vibrations in the sample. The peaks located at 855 cm^{-1}, 553 cm^{-1}, 471 cm^{-1}, and 443 cm^{-1} are attributed to the metal–oxide (M–O) bond. The Fe–O band of magnetite is characterized by a prominent absorption peak at around 553 cm^{-1}, while the peak at about 471 cm^{-1} shows the Fe–O bond of hematite.[39,40] The peaks located at around 443 cm^{-1} and 855 cm^{-1} can be assigned to Ni–O and Cr–O, respectively,[41,42] suggesting the formation of $NiCr_2O_4$; therefore, the FTIR analysis further verified the XRD, XPS, and EDX results.

3.2. Electrochemical performance of the SUS oxide electrode

The electrochemical behavior of the nanostructured SUS-304L oxide electrode was primarily investigated by CV

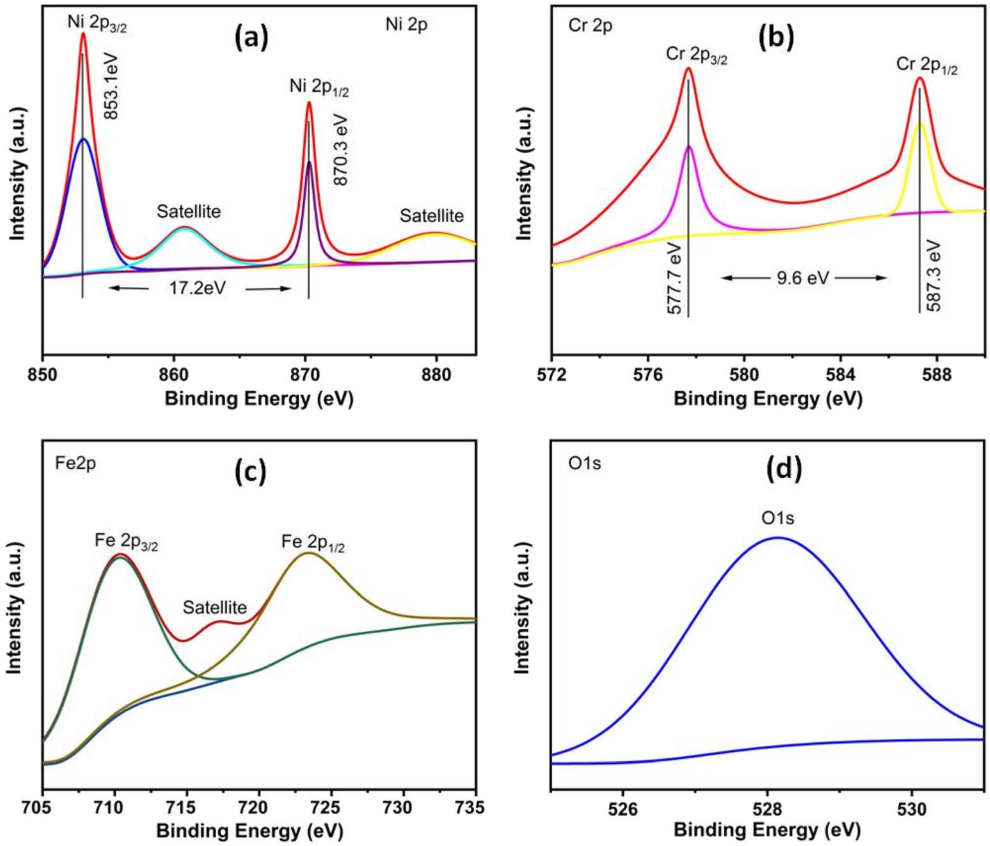

Fig. 5 High-resolution XPS spectra of the nanostructured SUS-304L oxide: (a) Ni 2p, (b) Cr 2p, (c) Fe 2p, and (d) O 1s.

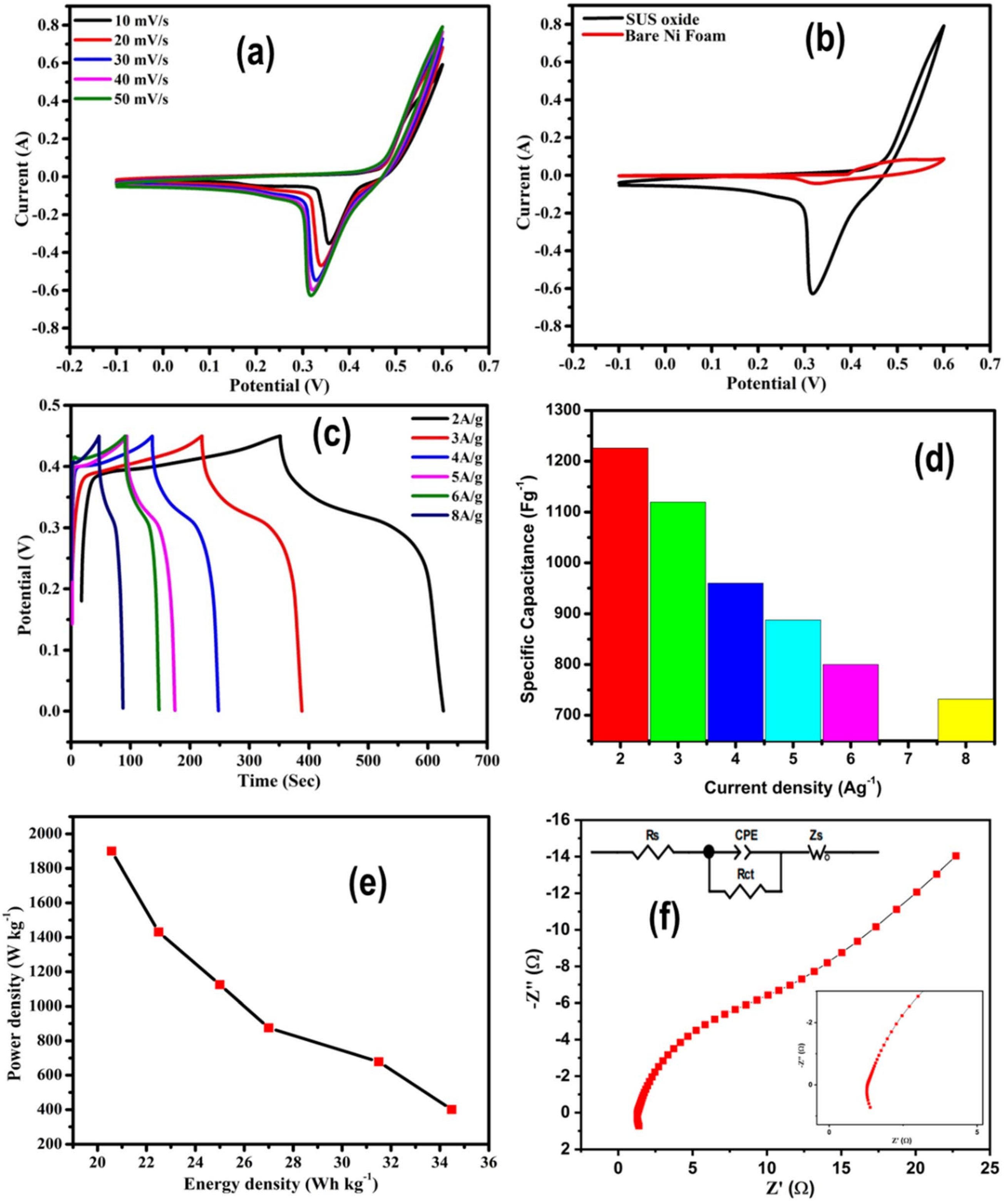

Fig. 6 (a) CV curves of the SUS-304L oxide at different scan rates (10–50 mV s^{-1}) in a potential window of −0.1 to 0.6 V. (b) CV curves of the bare Ni-foam and SUS-304L oxide electrode at 50 mV s^{-1}. (c) GCD curves at various current densities in the potential window of 1 to 0.5 V. (d) A graph of the capacitance *vs.* current density. (e) The cyclic stability graph. (f) The Nyquist plot at low and high magnifications.

measurements at different scan rates in the range of 10 to 50 mV s^{-1} in a voltage window of −0.1 to 0.6 V as shown in Fig. 6a. The appearance of anodic and cathodic peaks in the CV curves of the SUS-304L oxide electrode indicates that the origin of capacitance is mainly due to the surface redox reactions. Furthermore, no apparent change in the shape of the CV curves with increasing scan rate was observed, which shows the excellent reversibility and outstanding stability of the prepared electrode.[43] A noticeable peak shift with an increase in scan rate (Fig. 6a) is attributed to the internal resistance of the electrode.[44] Fig. 6b shows the CV curves of the bare Ni-foam, along with the fabricated electrode at 50 mV s^{-1}. It can be seen that the integrated area of the Ni-foam CV is much smaller compared to the nanostructured SUS-304L oxide electrode, showing its negligible role in capacitance contribution. The electrochemical performance of the nanostructured SUS-304L oxide electrode was further evaluated by GCD measurements. Fig. 6c shows the GCD curves of the electrode at different current densities ranging from 2 to 8 A g^{-1} in 1 M KOH electrolyte. The GCD curves did not change their shape with varying current density, confirming that the fabricated electrode has excellent stability, thus further verifying the CV results. Fig. 6d shows the calculated values of the specific capacitance, which are 1226, 1120, 960, 888, 800, and 732 F g^{-1} at current densities of 2, 3, 4, 5, 6, and 8 A g^{-1}, respectively. Interestingly, the SUS-304L oxide electrode delivered a high capacitance of ~1226 F g^{-1} at 2 A g^{-1} and maintained 732 F g^{-1} when the current density increased to 8 A g^{-1}. It clearly demonstrates that the specific capacitance of the electrode decreases with increasing current density. This is because at higher current densities, the movement of the electrolyte ions did not coordinate very well with the current rates.[44] The relationship between the electrode specific capacitance and current density revealed a decrease in the specific capacitance with increasing current density (Fig. 6d).

Energy density and power density are the two important factors in determining the suitability of any electrode material for commercial applications. The energy density and power density were calculated using the GCD curves. The nanostructured SUS-304L oxide electrode exhibited a maximum energy density of around 34.8 Wh kg^{-1} and a power density of about 400.4 W kg^{-1} at 2 A g^{-1}, with a maximum power density of ~1899.6 W kg^{-1} and energy density of approximately 20.58 Wh kg^{-1} at 8 A g^{-1} as given in Table 2. Fig. 6e presents the cyclic stability of the nanostructured SUS-304L oxide electrode, carried out for 8500 cycles at 8 A g^{-1}; it is clear that the nanostructured SUS-304L oxide electrode maintained a very stable performance during the long-term cycling test. It is worth mentioning that 92% capacitance retention was maintained at a high current density. The SUS-304L oxide electrode is implied to have an outstanding stability because of its high conductivity and less degradation after repeated charge–discharge cycles. Table 3 shows the electrochemical performance of the fabricated nanostructured SUS-304L oxide electrode compared with the reported electrodes.

Table 2 Capacitance and Ragone plot parameters of the fabricated SUS-304L oxide electrode

Current density (A g^{-1})	2	3	4	5	6	8
Specific capacitance (F g^{-1})	1226	1120	960	888	800	732
Energy density (Wh kg^{-1})	34.8	31.5	27	25	22.5	20.58
Power density (W kg^{-1})	400.4	678	875	1125	1431	1899

The electrochemical kinetics of the electrode were measured using EIS in the frequency range from 0.1 Hz to 140 kHz. Fig. 6f shows the Nyquist plot of the nanostructured SUS-304L oxide electrode, while the inset shows the fitted equivalent circuit that defines the Nyquist plot parameters. The Nyquist plot has three regions: an intercept on the real axis, which shows the solution resistance (R_s), the semicircle in the high frequency domain, which indicates the charge transfer resistance (R_{ct}) at the electrode/electrolyte interface, and the slope of the line, which determines the Warburg impedance. The R_s value (1.35 Ω) was calculated from the intersection of the curve on the real impedance axis (Z'), while the R_{ct} value (1.56 Ω) was obtained from the semicircle diameter. These smaller values of R_s and R_{ct} confirmed that the fabricated electrode has excellent conductivity and quick electrolyte ion transport features during the charge/discharge process.

3.3. The performance of the asymmetric supercapacitor (SUS-304L oxide//AC) device

In order to assess the practical application of the nanostructured SUS-304L oxide, an asymmetric supercapacitor device was fabricated (shown in the schematic diagram in Fig. 8a) using SUS-304L oxide as the anode, activated carbon (AC) as the cathode, a Whatman separator [(SUS-304L oxide//AC)], and PVA/KOH gel electrolyte.

The CV response of the device at various scan rates ranging from 10 to 50 mV s^{-1} in the potential window of 0 to 1.0 V is shown in Fig. 7a. It was observed that by increasing the scan rate, the current response increased without any change in the shape

Table 3 Comparative analysis of electrochemical performance of the fabricated SUS-304L oxide electrode with the previously reported electrodes

Active material	Electrolyte solution	Specific capacitance (F g^{-1})	Current density (A g^{-1})	Cyclic stability	References
CNT/Fe_2O_3	3 M KOH	512	1	85.5% after 2000 cycles	48
Fe_3O_4/graphene	1 M KOH	300	0.4	93% after 500 cycles	49
α-Fe_2O_3	0.5 M Na_2SO_3	193	1	92% after 1000 cycles	50
$NiCr_2O_4$	1 M KOH	422	0.6	80% after 2000 cycles	51
$Ni(OH)_2$@α-Fe_2O_3	1 M NaOH	908	21.8	85.7% after 5000 cycles	52
$Ni_{0.5}Co_{0.5}Fe_2O_4$	3 M KOH	213	4	98.7% after 1000 cycles	37
SUS-304L oxide nanostructure	**1 M KOH**	**1226**	**2**	**92% after 8500 cycles**	**This work**

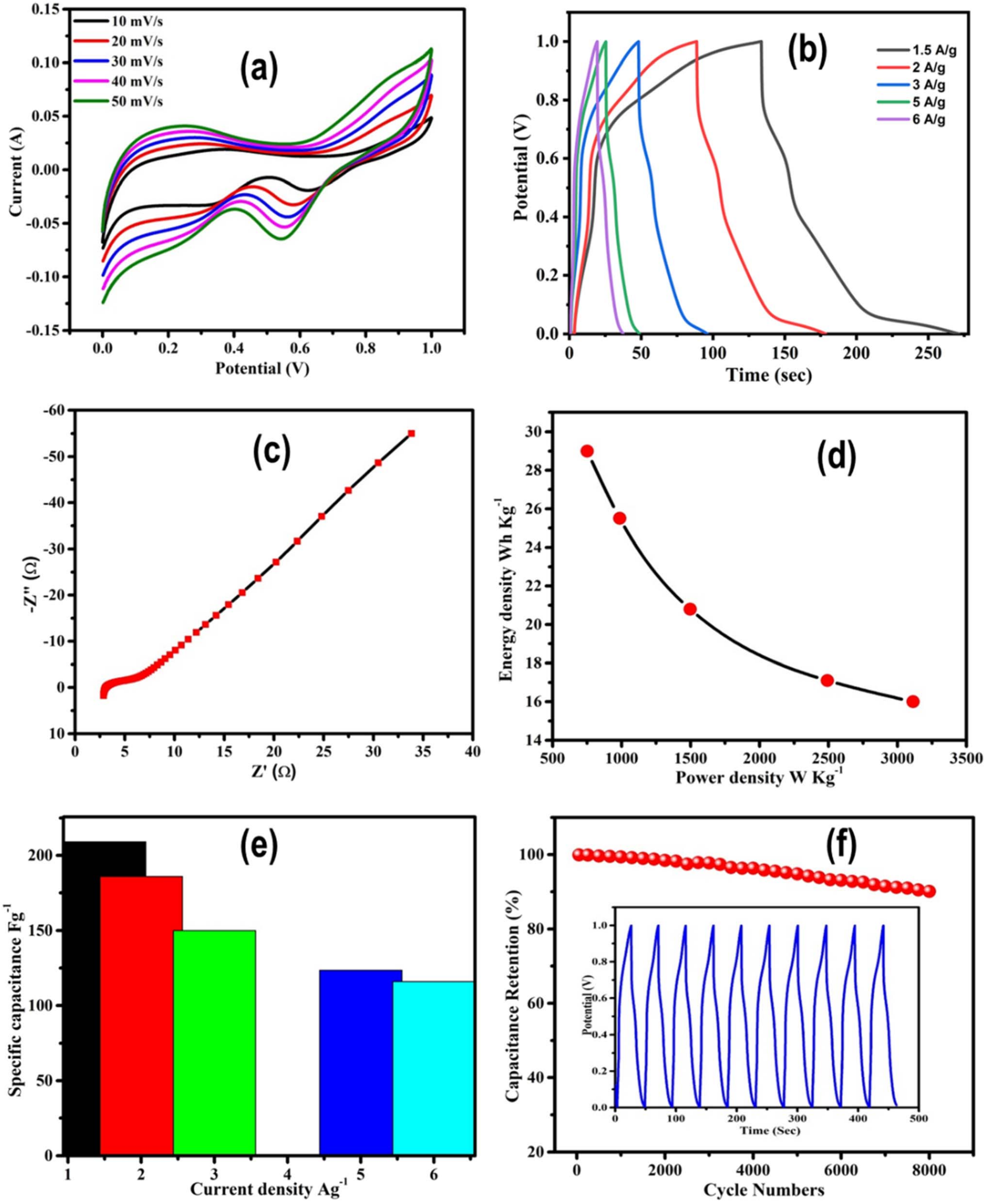

Fig. 7 (a) CV of SUS-304L oxide//AC at different scan rates ranging from 10–50 mV s^{-1} in a potential window of 1 V. (b) GCD curves at various current densities in a potential window of 1 V. (c) Nyquist plot. (d) Ragone plot between energy density and power density. (e) Graph of capacitance *vs.* current density. (f) Cyclic stability of the fabricated device.

Table 4 Capacitance and Ragone plot parameters of the fabricated ASC device

Current density (A g^{-1})	1.5	2	3	5	6
Specific capacitance (F g^{-1})	209	186	150	123.5	116
Energy density (Wh kg^{-1})	29	25.8	20.8	17.1	16
Power density (W kg^{-1})	751	987	1497	2492	3113

of the CV curves, suggesting excellent capacitive behavior. Fig. 7b shows the GCD curves measured at different current densities ranging from 2 to 6 A g^{-1} in a potential window of 0 to 1 V. The specific capacitance of the device at different current densities was calculated using GCD curves as displayed in Table 4. The formation of the nonlinear, triangular shape of the GCD curves indicates the outstanding efficiency and high reversibility of the fabricated device. Fig. 7b shows that the device exhibited a high specific capacitance of ~209 F g^{-1} at a current density of 1.5 A g^{-1}, and even at a higher current density (6 A g^{-1}), the ASC device (SUS oxide//AC) retained good capacitance, which is useful for long-term energy storage devices. Fig. 7c shows the Nyquist plot of the device, demonstrating enhanced kinetics. The smaller values of R_s (2.8 Ω) and R_{ct} (6.9 Ω) from the *x*-intercept support the fast mass transport and quick electrolyte ion diffusion into the electrode material's inner and outer surfaces. More significantly, during a working potential window (0–1.0 V), the ASC device showed an outstanding energy density of 29 Wh kg^{-1} at a power density of 751 W kg^{-1}, which indicates the importance of the nanostructured SUS-304L oxide in practical utilization for the supercapacitor applications. The energy density and power density of the fabricated device were evaluated using GCD curves (Table 4) and a Ragone plot (Fig. 7d). The specific capacitance against current density is displayed in the form of a bar graph in Fig. 7e. In order to investigate the durability and long-term cyclic stability, the device was tested for 8000 cycles at a high current density of 6 A g^{-1}, as shown in Fig. 7f. The cyclic stability for the first 10 cycles at a current density of 6 A g^{-1} is shown in the inset of Fig. 7f; the ASC device exhibited excellent stability with a capacity retention of about 89% after 8000 cycles.

To demonstrate the practical application of our fabricated device, we connected two (1 × 1 cm^2) devices in series, and their voltage (2.45 V) was checked using a voltmeter (see Fig. 8b); we observed that connecting in series increased the overall voltage. The different LED lights glowed when connected in series with our fabricated device, as shown in Fig. 8c and d. In contrast, connecting the device in parallel kept the voltage the same as a single device but increased the total capacitance, which boosted energy storage. These promising results suggest excellent energy storage behavior for the fabricated SUS-304L oxide//AC asymmetric supercapacitor.

3.4. Computational study

It was very interesting to investigate the origin of the high specific capacitance of the nanostructured SUS-304L oxide. The XRD data showed that the anodic SUS-304L oxide was mainly composed of Fe_2O_3, Fe_3O_4, and $NiCr_2O_4$, so we carried out *ab initio* calculations based on DFT within generalized gradient approximation (GGA)[45] to study the electronic structure of these oxides. The VASP[46] code with PAW pseudopotentials was used to describe the core electrons. All atoms were fully relaxed, and the convergence threshold on energy and forces for ionic minimization were taken as 10–4 eV and 1.5×10^{-2} eV $Å^{-1}$, respectively. Plane-wave cut-off energies of 400 eV, 600 eV, and 450 eV were used for Fe_2O_3, Fe_3O_4, and $NiCr_2O_4$, respectively. Dense mesh was used for density of states calculations using the tetrahedron method with Blöchl corrections.[47]

The calculated binding energies for Fe_2O_3, Fe_3O_4, and $NiCr_2O_4$ were −4.75, −4.61, and −6.52 eV, respectively. The negative values indicate the thermodynamic stability of these oxides, which is consistent with the XRD data. The charge density analyses (Fig. 9) showed that all these oxides have covalent bonding. The electronic structures of these oxides were also calculated, and it was revealed that these oxides prefer the spin-polarized band structures. The calculated spin-polarized orbital resolved densities of states are shown in Fig. 10. All these oxides are half metallic, where the spin-up (spin-down) states are metallic (insulating) in the case of $NiCr_2O_4$, and the

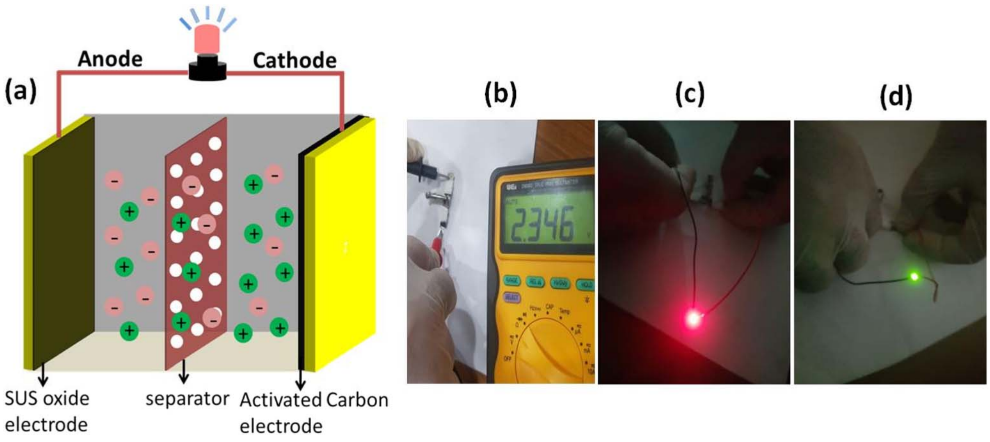

Fig. 8 (a) The inner-side charge-storage mechanism of the fabricated device. (b) The recorded voltage of the device. (c and d) The different colors (red and green) of LEDs turned ON when connected to the device.

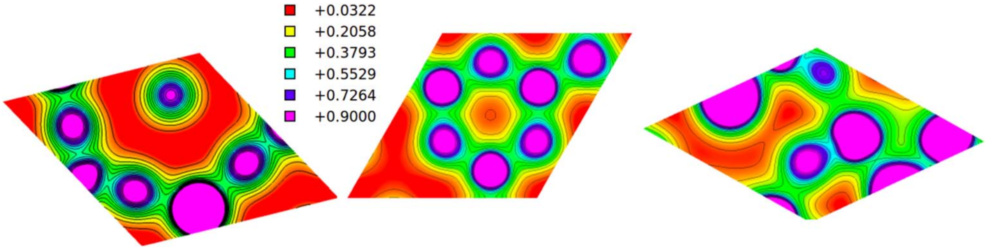

Fig. 9 DFT-calculated charge density of $NiCr_2O_4$ (left), Fe_3O_4 (middle), and Fe_2O_3 (right).

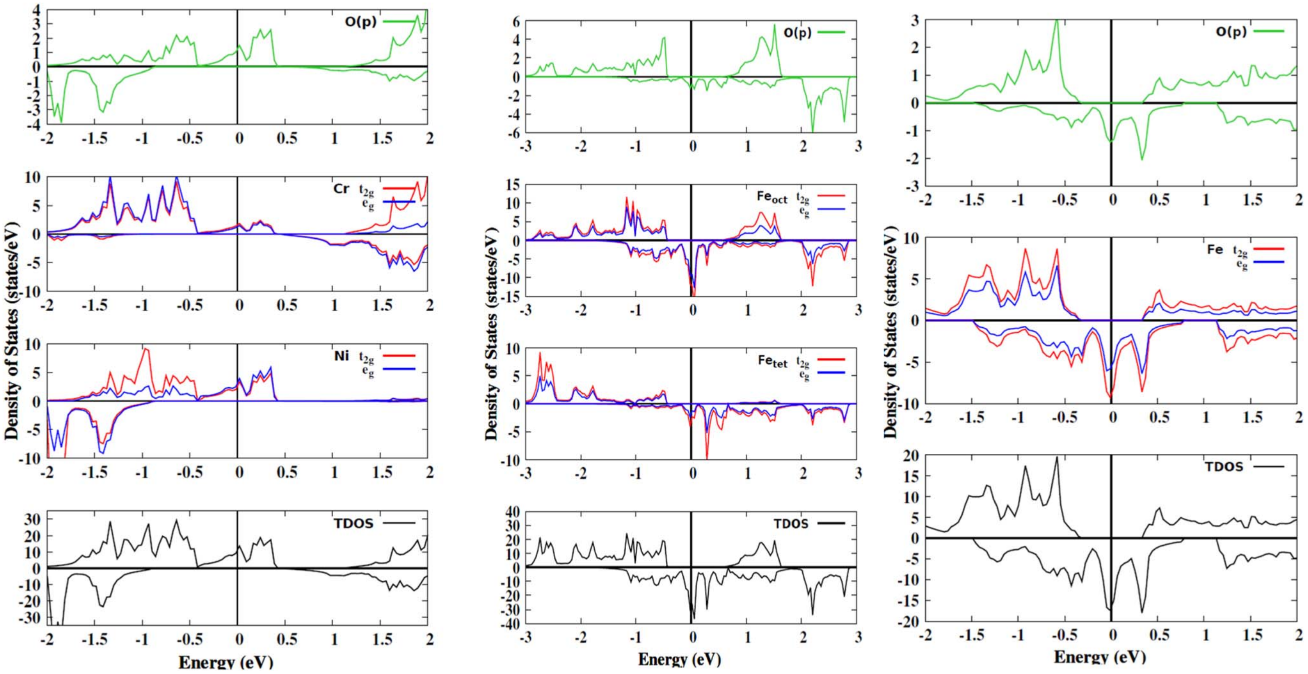

Fig. 10 DFT-calculated density of states of $NiCr_2O_4$ (left), Fe_3O_4 (middle), and Fe_2O_3 (right). The Fermi level is set to zero. The total density of state (TDOS) is shown in the lower panel. The positive (negative) DOS shows the spin-up (spin-down) states.

states close to the Fermi level were mainly contributed by the t_{2g} and e_g electrons of Cr and Ni. The O p-orbitals hybridized with the d orbitals of Cr and Ni. On the other hand, for Fe_2O_3 and Fe_3O_4, the spin-down states are metallic and the spin-up states are insulating. Note that Fe_3O_4 has two types of Fe atoms, *i.e.*, Fe atoms at the octahedral and tetrahedral sites. The t_{2g} and e_g orbitals in the spin-up states are almost occupied at the tetrahedral site, whereas they are partially occupied at the octahedral site. Large densities of states due to the t_{2g} and e_g orbitals of octahedral Fe at the Fermi energy were observed.

Using the density of states, the quantum capacitance of the nanostructured SUS-304L oxide was calculated. The quantum capacitance of Fe_2O_3, Fe_3O_4, and $NiCr_2O_4$ were calculated at different voltages, and the calculated quantum capacitance is shown in Fig. 11. On analyzing the quantum capacitance values for these oxides at different potentials, it was observed that Fe_2O_3 and Fe_3O_4 have high quantum capacitance values at zero potential but drastically decreased as potential increased, up to 0.2 V; on further increasing the potential, the quantum capacitance increased. The quantum capacitances of Fe_2O_3 and Fe_3O_4 exhibited symmetrical behavior, whereas $NiCr_2O_4$ had asymmetrical behavior. Under a negative voltage, Fe_2O_3 has a larger capacitance than Fe_3O_4. The calculated quantum capacitance

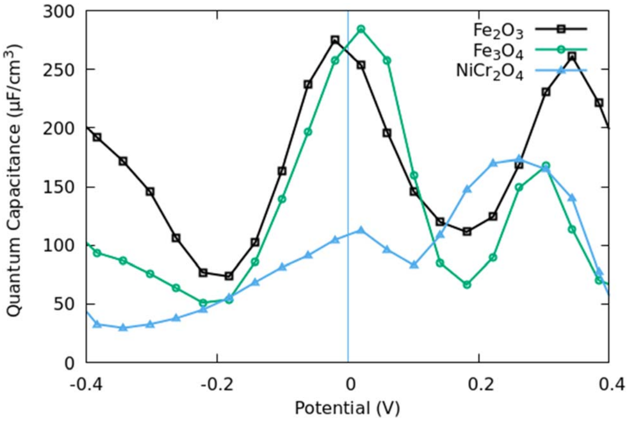

Fig. 11 Quantum capacitance of Fe_2O_3 (filled squares), Fe_3O_4 (filled circles), and $NiCr_2O_4$ (filled triangles).

increased with voltage because the density of states increased as the Fermi level moved into regions with higher DOS. Thus, we conclude that the large specific capacitance of SUS-304L oxide, mainly contributed by Fe-oxides, can be attributed to the large density of states of the minority spin states of the t_{2g} and e_g orbitals of Fe atoms at the octahedral site.

3.5. Conclusion

This article presents the successful fabrication of a novel nanostructured SUS-304L oxide (powder form) for supercapacitor applications using a simple, cost-effective, and rapid anodization technique. Structural and microscopic analyses revealed the formation of multiple phases and spherical NPs overlapping 2D NSs with a unique morphology. Electrochemical measurements in a three-electrode configuration demonstrated the pseudocapacitive behavior of the SUS-304L oxide electrode, achieving a high specific capacitance of about 1226 F g^{-1} at a current density of 2 A g^{-1} with excellent reversibility. The fabricated asymmetric supercapacitor device (SUS-304L oxide//AC) exhibited a remarkable specific capacitance of 209 F g^{-1} at 1.5 A g^{-1}, and an energy density of 29 Wh kg^{-1} at a power density of 751 W kg^{-1}. Moreover, the device maintained 89% of its specific capacitance at 6 A g^{-1} and outstanding cyclic stability up to 8000 cycles. *Ab initio* calculations based on DFT were used to determine the quantum capacitance of Fe_2O_3, Fe_3O_4, and $NiCr_2O_4$. The calculated binding energies have negative values—indicating the thermodynamic stability of these oxides. The electronic structures show the half-metallic nature of these oxides. The observed large capacitance is mainly contributed by Fe-oxides, and can be attributed to the large density of states of the minority spin states of t_{2g} and e_g orbitals of Fe atoms at the octahedral sites. These results establish the SUS-304L oxide nanostructure as a strong candidate for next-generation energy storage devices.

Author contributions

G. A. conceived the idea; J. A. and M. D. designed the study and carried out the experiments; and S. C. and Y. Xie helped in characterizing and interpreting the results. G. A., J. A., and M. D. analyzed the experimental data and its interpretation. J. A. and M. D. prepared the initial draft of the manuscript. G. R. carried out DFT calculations and completed the computational write-up. M. A., M. K., and S. A. revised the initial draft and helped improve it with their technical contributions. G. A. and S. O. C. funded the study and supervised the project. All authors were involved in the discussion and drafting of the manuscript. J. A. and G. A. finalized the revised manuscript with inputs and comments from all authors.

Conflicts of interest

The authors declare that they have no known competing financial interests or personal relationships that could have influenced the work reported in this study.

Data availability

The data supporting this article have been included in the main text of the manuscript as well as part of the supplementary information (SI). Supplementary information: schematic of nanostructured SUS-304L oxide synthesis *via* anodization along with electrochemical setup, schematic of the fabricated device, XPS survey scans, and FTIR spectrum of nanostructured SUS-304L oxide. See DOI: **https://doi.org/10.1039/d5na00618j**.

Acknowledgements

This work was supported by Ministry of Science and ICT (MSIT) of the Republic of Korea through the Radiation Innovation Utilization Technology Development Program (grant number: RS-2025-02653965). The author (Ghafar Ali) also greatly acknowledge PINSTECH, Pakistan for providing financial support for this research work.

References

1 G. Wang, L. Zhang and J. Zhang, A review of electrode materials for electrochemical supercapacitors, *Chem. Soc. Rev.*, 2012, **41**(2), 797–828.

2 C. Liu, *et al.*, Advanced materials for energy storage, *Adv. Mater.*, 2010, **22**(8), E28–E62.

3 P. Nagaraju, *et al.*, Facile in-situ microwave irradiation synthesis of TiO2/graphene nanocomposite for high-performance supercapacitor applications, *J. Electroanal. Chem.*, 2018, **808**, 90–100.

4 C. Xiang, *et al.*, Reduced graphene oxide/titanium dioxide composites for supercapacitor electrodes: shape and coupling effects, *J. Mater. Chem.*, 2012, **22**(36), 19161–19167.

5 V. Sharavath, S. Sarkar and S. Ghosh, One-pot hydrothermal synthesis of TiO2/graphene nanocomposite with simultaneous nitrogen-doping for energy storage application, *J. Electroanal. Chem.*, 2018, **829**, 208–216.

6 A. Borenstein, *et al.*, Carbon-based composite materials for supercapacitor electrodes: a review, *J. Mater. Chem. A*, 2017, **5**(25), 12653–12672.

7 Y. Liu, X. Xu and Z. Shao, Metal-organic frameworks derived porous carbon, metal oxides and metal sulfides-based compounds for supercapacitors application, *Energy Storage Mater.*, 2020, **26**, 1–22.

8 X. Li, *et al.*, Metal phosphides and phosphates-based electrodes for electrochemical supercapacitors, *Small*, 2017, **13**(39), 1701530.

9 T. Nguyen and M. d. F. Montemor, Metal oxide and hydroxide–based aqueous supercapacitors: from charge storage mechanisms and functional electrode engineering to need-tailored devices, *Advanced Science*, 2019, **6**(9), 1801797.

10 T. Yue, *et al.*, Design and synthesis of conductive metal-organic frameworks and their composites for supercapacitors, *ChemElectroChem*, 2021, **8**(6), 1021–1034.

11 S. D. Dhas, *et al.*, Synthesis of NiO nanoparticles for supercapacitor application as an efficient electrode material, *Vacuum*, 2020, **181**, 109646.

12 Y. Xiao, *et al.*, A comparative study of one-dimensional and two-dimensional porous CoO nanomaterials for asymmetric supercapacitor, *J. Alloys Compd.*, 2019, **781**, 1006–1012.

13 R. Arunachalam, *et al.*, Pulse electrodeposited RuO2 electrodes for high-performance supercapacitor applications, *Surf. Eng.*, 2019, **35**(2), 102–108.

14 P. M. Kulal, *et al.*, Chemical synthesis of Fe2O3 thin films for supercapacitor application, *J. Alloys Compd.*, 2011, **509**(5), 2567–2571.

15 D. P. Dubal, *et al.*, CuO cauliflowers for supercapacitor application: Novel potentiodynamic deposition, *Mater. Res. Bull.*, 2013, **48**(2), 923–928.

16 A. G. Temam, *et al.*, Recent progress on V2O5 based electroactive materials: Synthesis, properties, and supercapacitor application, *Curr. Opin. Electrochem.*, 2023, **38**, 101239.

17 N. Kandasamy, T. Venugopal and K. Kannan, Facile one-pot synthesis of flower like cobalt oxide nanostructures on nickel plate and its supercapacitance properties, *J. Nanosci. Nanotechnol.*, 2018, **18**(6), 3960–3968.

18 N. Jabeen, *et al.*, High-performance 2.6 V aqueous asymmetric supercapacitors based on in situ formed Na0. 5MnO2 nanosheet assembled nanowall arrays, *Adv. Mater.*, 2017, **29**(32), 1700804.

19 G. C. Mohanty, *et al.*, Iron-cobalt-nickel-copper-zinc (FeCoNiCuZn) high entropy alloy as positive electrode for high specific capacitance supercapacitor, *Electrochim. Acta*, 2023, **470**, 143272.

20 G. C. Mohanty, *et al.*, High energy density liquid state asymmetric supercapacitor devices using Co–Cr–Ni–Fe–Mn high entropy alloy, *Mater. Adv.*, 2023, **4**(17), 3839–3852.

21 T. Motsei, K. G. Tshabalala and R. O. Ocaya, Composite super-capacitor/Na-ion battery with self-healing Fe–Cr alloy electrodes, *Phys. B*, 2023, **671**, 415384.

22 M. Deyab, *et al.*, Progress study on nickel ferrite alloy-graphene nanosheets nanocomposites as supercapacitor electrodes, *J. Energy Storage*, 2022, **46**, 103926.

23 G. Ali, *et al.*, Formation of hexagonally-ordered zircaloy oxide nanostructures with different morphologies using two-step anodization, *J. Alloys Compd.*, 2015, **640**, 205–209.

24 G. Ali, *et al.*, Controlled fabrication of porous double-walled TiO 2 nanotubes via ultraviolet-assisted anodization, *Nanoscale*, 2014, **6**(7), 3632–3637.

25 G. Ali, *et al.*, Rapid synthesis of TiO2 nanoparticles by electrochemical anodization of a Ti wire, *Nanotechnology*, 2013, **24**(18), 185601.

26 A. Hassan, *et al.*, Formation of a self-organized nanoporous structure with open-top morphology on 304L austenitic stainless steel, *Nanotechnology*, 2020, **31**(31), 315603.

27 G. Ali, *et al.*, A green, general, and ultrafast route for the synthesis of diverse metal oxide nanoparticles with controllable sizes and enhanced catalytic activity, *ACS Appl. Nano Mater.*, 2018, **1**(11), 6112–6122.

28 A. Hassan, *et al.*, Formation of highly-ordered and hexagonal nanoporous structure on the surface of 304L austenitic stainless steel, *Nanotechnology*, 2020, **31**, 315603.

29 N. Khaliq, *et al.*, Voltage-switchable biosensor with gold nanoparticles on TiO2 nanotubes decorated with CdS quantum dots for the detection of cholesterol and H2O2, *ACS Appl. Mater. Interfaces*, 2021, **13**(3), 3653–3668.

30 B. Mordina, *et al.*, Binder free high performance hybrid supercapacitor device based on nickel ferrite nanoparticles, *J. Energy Storage*, 2020, **31**, 101677.

31 A. J. Bard, L. R. Faulkner and H. S. White, *Electrochemical Methods: Fundamentals and Applications*, John Wiley & Sons, 2022.

32 G. Ali, *et al.*, A novel route to the formation of 3D nanoflower-like hierarchical iron oxide nanostructure, *Nanotechnology*, 2019, **30**(9), 095601.

33 H. Ullah, *et al.*, A sensitive non-enzymatic glucose sensor based on MgO entangled nanosheets decorated with CdS nanoparticles: experimental and DFT study, *J. Mol. Liq.*, 2022, **360**, 119366.

34 L. S. Zhong, *et al.*, Self-Assembled 3D flowerlike iron oxide nanostructures and their application in water treatment, *Adv. Mater.*, 2006, **18**(18), 2426–2431.

35 P. Mohanty, *et al.*, Effect of Fe substitution on structural and magnetic properties of $NiCr_2O_4$, *Acta Phys. Pol. A*, 2018, **133**(3), 574–577.

36 M. Sathyan, *et al.*, Electrode material for high performance symmetric supercapacitors based on superparamagnetic Fe3O4 nanoparticles modified with cetyltrimetylammonium bromide, *Synth. Met.*, 2022, **287**, 117080.

37 J. Halder, *et al.*, Bricks of Co, Ni doped Fe3O4 as high performing pseudocapacitor electrode, *J. Energy Storage*, 2023, **58**, 106391.

38 S. Sobhanardakani, *et al.*, Removal of heavy metal (Hg (II) and Cr (VI)) ions from aqueous solutions using Fe2O3@ SiO2 thin films as a novel adsorbent, *Process Saf. Environ. Prot.*, 2018, **120**, 348–357.

39 D. Shanthini Keerthana and K. Namratha Kand Byrappa, Green Hydrothermal Synthesis of Magnetite Nanoparticles and their Free Radi-cal Scavenging Property, *BAOJ Physics*, 2017, **2**, 012.

40 A. H. Farha, *et al.*, Novel Magnetite (Fe3O4)-Methylcellulose Nanocomposites Synthesized Using the Reverse Co-Precipitation Approach, *J. Compos. Sci.*, 2024, **8**(7), 282.

41 V. Vats, *et al.*, FTIR spectroscopy as a convenient tool for detection and identification of airborne Cr (VI) compounds arising from arc welding fumes, *J. Hazard. Mater.*, 2023, **448**, 130862.

42 S. D. Khairnar and V. S. Shrivastava, Facile synthesis of nickel oxide nanoparticles for the degradation of Methylene blue and Rhodamine B dye: a comparative study, *J. Taibah Univ. Sci.*, 2019, **13**(1), 1108–1118.

43 S. Abbas, *et al.*, Zn doping induces rich oxygen vacancies in δ-MnO2 flower-like nanostructures for impressive energy density coin cell supercapacitor, *J. Energy Storage*, 2024, **87**, 111455.

44 H. S. Chavan, *et al.*, Nanoflake NiMoO4 based smart supercapacitor for intelligent power balance monitoring, *Sol. Energy Mater. Sol. Cells*, 2018, **185**, 166–173.

45 J. P. Perdew, K. Burke and M. Ernzerhof, Generalized gradient approximation made simple, *Phys. Rev. Lett.*, 1996, **77**(18), 3865.

46 G. Kresse and J. Furthmüller, Efficiency of ab-initio total energy calculations for metals and semiconductors using a plane-wave basis set, *Comput. Mater. Sci.*, 1996, **6**(1), 15–50.

47 P. E. Blöchl, Projector augmented-wave method, *Phys. Rev. B:Condens. Matter Mater. Phys.*, 1994, **50**(24), 17953.

48 K. Ponnarasi, P. Elangovan and S. Surender, Development of CNT/Fe2O3 nanocomposites as electrode materials for advanced supercapacitors, *Results Chem.*, 2024, **7**, 101355.

49 J. Liao, *et al.*, In-situ preparation of Fe3O4/graphene nanocomposites and their electrochemical performances for supercapacitor, *Mater. Chem. Phys.*, 2021, **258**, 123995.

50 S. Shivakumara, T. R. Penki and N. Munichandraiah, Preparation and electrochemical performance of porous hematite (α-Fe 2 O 3) nanostructures as supercapacitor electrode material, *J. Solid State Electrochem.*, 2014, **18**, 1057–1066.

51 X. Xu, J. Gao and W. Hong, Ni-based chromite spinel for high-performance supercapacitors, *RSC Adv.*, 2016, **6**(35), 29646–29653.

52 W. Tian, *et al.*, Ni (OH) 2 nanosheet@ Fe2O3 nanowire hybrid composite arrays for high-performance supercapacitor electrodes, *Nano energy*, 2013, **2**(5), 754–763.